RSC Advances

ROYAL SOCIETY OF CHEMISTRY

PAPER

View Article Online
View Journal | View Issue

Cite this: *RSC Adv.*, 2025, **15**, 142

Effect of electrodeposition time on physical characteristics and antibacterial activity of copper-incorporated TiO_2 nanotubes†

Justynne Fabian, *[a] Grant Morton,[b] Shubham Sharma, [a] Brendan Duffy [a] and Susan Warren *[a]

The current work outlines the preparation of a TiO_2 nanotube (NT) layer electrochemically formed on the surface of a clinically-relevant titanium alloy *via* anodisation. This NT layer was subsequently modified *via* alternating current electrodeposition to incorporate copper micro- and nanoparticles on top of and within the NTs. Physical characterisation of the NT layer and the copper-incorporated NTs was carried out through analysis of the surface morphology, elemental composition, crystallinity, and stability *via* SEM, EDX, XRD, and ICP-OES, respectively. After immersion in Dulbecco's phosphate buffer saline solution at 37 °C for 24 hours, the electrodeposited copper particles transformed into $Cu_3(PO_4)_2 \cdot 3H_2O$ microflowers. Bacterial susceptibility tests were carried out against *E. coli* and *S. aureus*. The antibacterial activity was influenced by the physical characteristics of the electrodeposited copper, the transformation of the copper particles to microflowers, and the extent at which the copper-incorporated surface released Cu^{2+} ions.

Received 19th July 2024
Accepted 11th December 2024

DOI: 10.1039/d4ra05266h

rsc.li/rsc-advances

1. Introduction

An effective strategy for improving a potential biomedical implant surface is the incorporation of antibacterial properties while retaining an osteoinductive environment. High concentrations of bactericidal agents, including antibiotics, can be cytotoxic and may interfere with osteogenesis. One approach is to introduce bactericidal agents before incorporating osteoinductive agents.[1,2] For an antimicrobial implant to be effective, it is essential to maintain bactericidal activity throughout the treatment period to prevent long-term implant-associated infections (IAIs).[3] This paper investigated the relationship between electrodeposition time and the physiochemical properties of the copper particles deposited on nanotubular surfaces through alternating current (AC) electrodeposition. Subsequently, the research examined how these characteristics influenced the antibacterial activity against *E. coli* and *S. aureus*, two prevalent bacterial strains responsible for IAIs.

Copper-based coatings have gained popularity as broad-spectrum antimicrobial agents.[4,5] While the precise mechanism of action is still debated, it is widely accepted that direct contact between bacteria and the copper surface leads to bacterial cell death *via* modification of the bacterial cell membrane. Additional mechanisms related to direct contact killing involve the generation of reactive oxygen species (ROS), which are induced by the formation of Cu^+ ions from Cu^{2+} ions. Cu^+ ions react with atmospheric oxygen, resulting in ROS formation, which damages intracellular components.[6] In addition to membrane disruption and ROS generation, DNA damage and inhibition of essential enzymes also contribute to the antibacterial activity of copper surfaces.[7–9]

As bacterial attachment to surfaces is a critical precursor to biofilm formation and subsequent infection, it is essential that the surface area be modified to discourage adherence. Studies suggest that nano/micro porosity on copper-incorporated surfaces may play a role in this process, with bacterial attachment inhibition depending on the surface morphology and the area exposed by the deposited copper.[10,11]

IAIs are a significant healthcare challenge[3,12] and a leading cause of hip implant failure.[13] Pathogenic bacteria responsible for IAIs have developed strategies for antimicrobial resistance.[14] These include the modification of target bacteria in response to antibacterial agents, such as the adaptation of membrane efflux pumps, which can selectively evade the intracellular accumulation of copper ions or copper nanoparticles.[14]

Nanostructured surfaces, or surfaces with nanoscale features, are often modified to incorporate antibacterial or biological activity.[15–17] The introduction of surface roughness and nanomorphology through anodisation of titanium to form TiO_2 nanotubes (NTs) has shown promise in fabricating biomedical implant surfaces with antibacterial properties.[18]

[a]*Centre for Research in Engineering Surface Technology (CREST), Technological University Dublin, City Campus, Kevin Street, Dublin 8, Ireland. E-mail: justynnefabian@gmail.com; swarren747@gmail.com*

[b]*Technological University Dublin, City Campus, Grangegorman, Dublin, Ireland*

† Electronic supplementary information (ESI) available. See DOI: https://doi.org/10.1039/d4ra05266h

Moreover, anodisation is a cost-effective and convenient method for producing TiO_2 NTs.

The anodisation of titanium to produce TiO_2 NTs typically involves a two-electrode electrochemical cell, with titanium as the anode. Four generations of TiO_2 NTs have been developed, with the fourth generation NTs being highly ordered through the use of organic solvents such as ethylene glycol, low water content (below 10%), and high applied voltages up to 60 V.[19,20] To enhance fourth-generation NTs, process parameters are often fine-tuned, although this can make the process more hazardous and less economical. For instance, electrolyte ageing is an important consideration, with some reports suggesting a 60 hour ageing process under a constant potential of 60 V to increase solution conductivity and NT length.[19]

The current work avoids the use of harsh conditions that are typically used in fourth generation NTs. Aqueous-based electrolytes are used in this work, at ambient experimental temperature and voltage, as well as avoiding the use of hazardous organic solvent. The employed anodisation method results in the formation of ordered TiO_2 NTs, which are known to have inherent antibacterial properties,[7] while the electrodeposition method makes use of the highly ordered nanotubular layer and results in the deposition of antibacterial metal particles on and within the NTs.

Copper was employed as the antibacterial agent, where the shape, size and distribution of the copper particles are investigated. As noted by Roguska *et al.*,[21] the preparation method highly affects the subsequent physicochemical properties of potential antibacterial nanoparticles, which can lead to varied bactericidal effects. The physicochemical properties of the copper particles are explored in this work through examination of the various morphologies achieved through variation of electrodeposition duration. Consequently, the compositional stability and leaching rates of the Cu^{2+} ions were investigated following immersion of the copper-incorporated NTs in Dulbecco's phosphate buffer saline (DPBS) solution over 24 hours. Following this, the effect of electrodeposition time was explored through monitoring changes in the physical characteristics of the metal particles, as well as monitoring the resulting antibacterial behaviour against Gram-positive and Gram-negative bacteria that are typically responsible for IAIs.

2. Results and discussion

Recently, an investigation was carried out to assess how different surface treatments on titanium foils affect the deposition of copper particles in terms of the particle shape and sizes.[11] The variation in the electrodeposition time was investigated to observe if there were any changes in the physical Cu characteristics which may be influenced by the two different Ti substrate surfaces: "Ti" surfaces refer to bare, unanodised Ti alloy surfaces, and "NT" refers to a Ti substrate that was anodised to form amorphous TiO_2 NTs. By providing a nanostructured template, it was hypothesised that changes in Cu deposited particles would already be influenced by the vertically aligned NT layer, and so be independent of Cu electrodeposition time. However, that was not the case. Longer deposition times were unfavourable as delamination of the copper particles, which start to rapidly attach and deposit on top of each other, occurs during the electrodeposition process. With times exceeding 90 s, the delamination of the copper particles also cause the removal of the underlying NT layer. So while fine-tuning of the particles' physical characteristics was shown to be possible at ambient experimental conditions such as low voltages and at a reasonably short experimental duration, there was certainly an observed upper limit in how much Cu can be deposited before breakdown of both the TiO_2 NT and Cu particle structures.

2.1 Surface morphology and elemental composition

The morphology of the electrodeposited copper particles varied with the electrodeposition duration. Below exhibits SEM images of three different surfaces, where the control is the nanotubular (NT-Control) layer as shown in Fig. 1(a). NT-Control is compared to an electrodeposited copper surface in the absence of a NT layer. The copper particles are consistently globular with particle sizes of 191 $\pm$ 22 nm with individual particles agglomerating in 3 μm clusters. Such large clusters are in contrast to electrodeposited NT surfaces, where the copper particles are smaller in diameter (62 $\pm$ 7 nm) with smaller clusters of 227 $\pm$ 22 nm. There is a larger variation in the copper particle shapes, ranging from rods to spherical shapes.

The NT-Control confirms the presence of Ti, Al, V, and O, which are accounted for due to the alloy used and the composition of the NT layer. With the electrodeposition of Cu onto the surface, the reduction in the intensity of the Ti, Al and V are especially noted, which indicates the extent at which the copper particles have covered the TiO_2 NT surface. A low distribution of copper is observed at 30 s deposition (NT/Cu 30) and this is supported with a comparatively low copper content of 45 $\pm$ 2 wt%. This observation suggests that the distribution of the copper particles increases with increasing duration, and that more copper is reduced at the NT surface than removed during electrodeposition. At 60 s, the surface copper for Ti/Cu 60 and NT/Cu 60 are 58 $\pm$ 3 and 53 $\pm$ 3 wt%, respectively, suggesting that the nature of the metal substrate that the deposition occurs on does not affect the amount of copper that is deposited. However, the presence of a small sulphur EDX peak (<5 wt%, ESI†) observed only for NT/Cu 30 and NT/Cu 60 originates from the electrolyte (copper(II) sulphate). Electrodeposition duration of 90 s results in an even higher increase in the Cu content, as shown in Fig. 1(e), where NT/Cu 90 presents a surface Cu content of 67 $\pm$ 6 wt%.

After electrodeposition, the copper particles on the NT surfaces are in the form of copper metal which adopt various morphologies that are influenced by the electrodeposition time and the underlying substrate morphology. Ti/Cu 60 exhibits copper particles with largely globular deposits. It is expected that these particles are not well-adhered to the titanium surface, as the absence of the NT layer means that the copper deposits, which are positively charged, are only loosely associated with the bare Ti metal surface. Despite pickling the Ti surface to limit the spontaneous formation of the native TiO_2 layer,

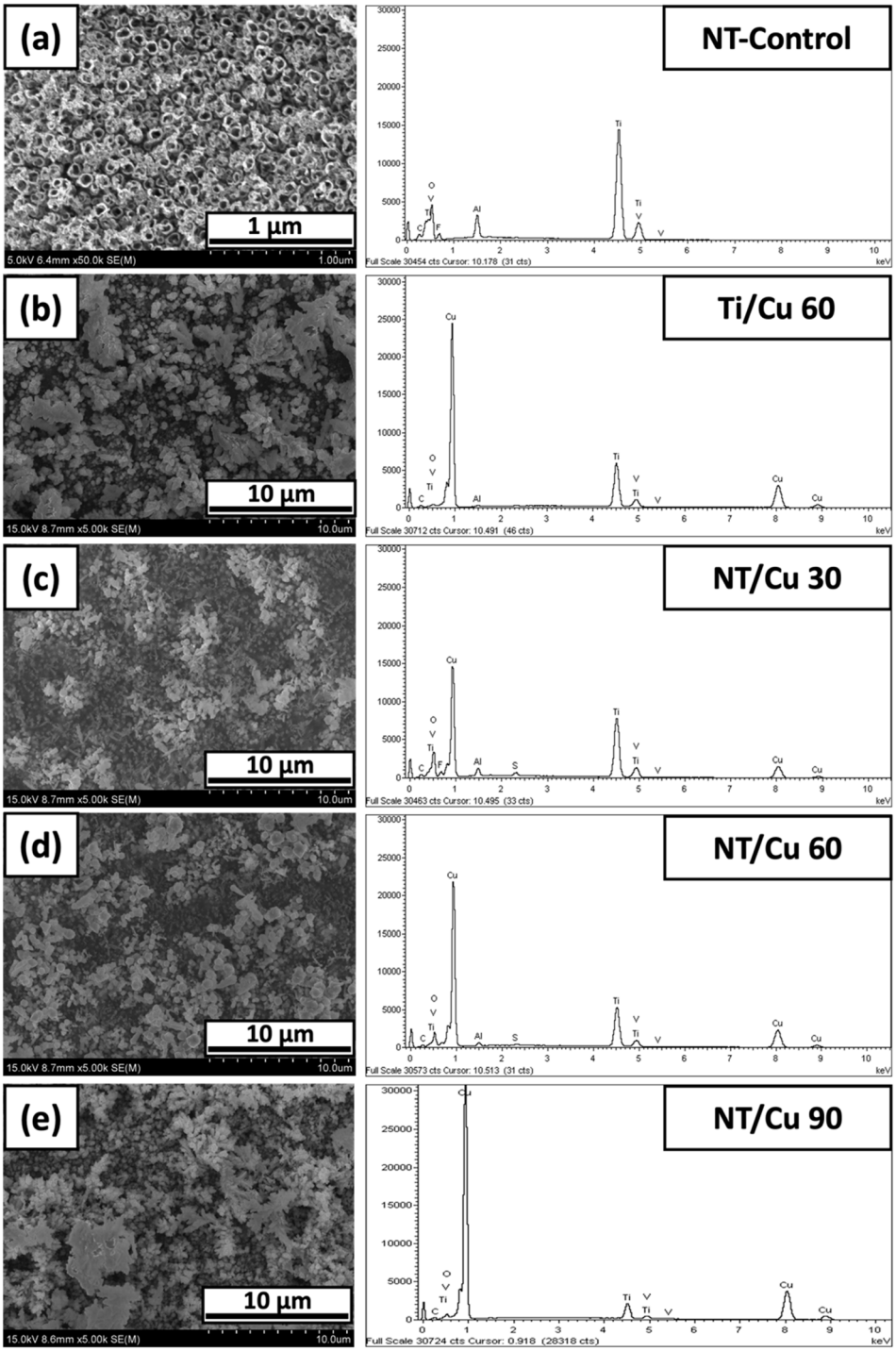

Fig. 1 SEM images and accompanying EDX spectra of NT-Control (a), (b) Ti/Cu 60, (c) NT/Cu 30, (d) NT/Cu 60, and (e) NT/Cu 90.

introduction of some negative charge afforded by the oxide layer may provide some electrostatic interaction between the Ti surface and the electrodeposited copper.

The electrostatic interaction between the substrate surface and the copper particles is more strongly influenced by the presence of a negatively-charged TiO_2 NT layer.[22] Due to the structure of the NTs, O^{2-}, OH^- and F^- anions are situated within the pores of the NT.[23] To further investigate how the copper particles are deposited within the NTs, adhesive tape was used to remove the top layer of Cu particles as well as the upper portion of the NT layer. The SEM images of the resulting Cu particles are shown in Fig. 2. It is noted that the structural integrity of the NTs remains intact.

As for Ti/Cu 60, the majority of the electrodeposited copper is removed, leaving behind a low distribution of spherical copper particles adhered to the Ti surface. In Fig. 2(b) and (c), NT/Cu 30

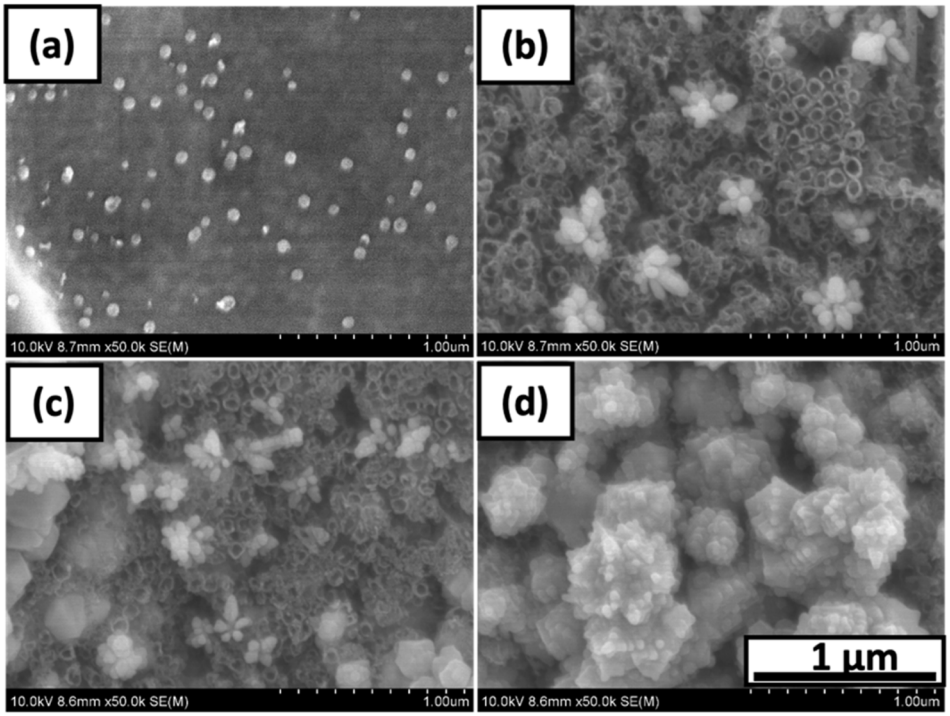

Fig. 2 SEM images of (a) Ti/Cu 60, (b) NT/Cu 30, (c) NT/Cu 60, (d) NT/Cu 90 after removal of top layer with tape.

and NT/Cu 60 feature clusters consisting of spherical particles that are 99.87 ± 14.35 nm and 61.65 ± 6.6 nm in diameter, respectively. The particles are of a similar size to the pores of the NTs, which are 65.13 ± 7.64 nm in diameter. While NT/Cu 30 exclusively features these clusters of Cu nanoparticles, NT/Cu 60 exhibits additional particle shapes which are larger than the clusters. These particles form larger clusters at 227 ± 22 nm. NT/Cu 90 (Fig. 2(d)) exhibits small, spherical particles that form clusters that appear to tend to polyhedral shapes, which completely cover the surface even after application of tape. The size of these cluster of spherical particles are 132 ± 11 nm, which are significantly larger than the NT pores. It would be expected that due to the high concentration of copper deposits following 90 s electrodeposition that the particles would be loosely adhered. The high copper content is supported by EDX data (Table 1), which show that NT/Cu 90 had a significantly higher Cu wt% content (67 ± 6 wt% Cu) compared to Ti/Cu 60 (58 ± 3 wt% Cu), NT/Cu 30 (45 ± 2 wt% Cu) and NT/Cu 60 (53 ± 3 wt% Cu). The particle sizes and the Cu content also play a role in the amount of Cu^{2+} ions leached.[24] This was evident with NT/Cu 60 which was found to have the lowest concentration of Cu^{2+} ion released (123 ± 19 ppb), as well as the smallest particle (62 ± 7 nm) and cluster size distributions. This observation could be attributed to the comparable size of the Cu spherical particles, the Cu content (53 wt%), and the NT pores within which the Cu particles are electrostatically attached to. The reverse was observed for NT/Cu 90, where the longest electrodeposition time resulted in the highest amount of Cu^{2+} ions released (161 ppb) which is attributed to larger particle sizes (132 nm) and a higher Cu content (67 wt%).

XRD analysis (Fig. 3) of samples from Fig. 1, exhibit crystalline Ti peaks (DB card 1532765: COD) at 2θ values of 35.91°, 39.03°, 41°, 53.81°, and 64.04°, which are attributed to the diffraction planes (101), (002), (101), (102), and (110), respectively. Diffraction due to the presence of copper metal is observed through the appearance of peaks at 2θ values 44° and 51° (DB card 9008468: COD), which correspond to diffraction planes (111) and (200), respectively. For NT/Cu 90, the additional peak at 36.96° denotes the formation of Cu_2O (DB card 9005769: COD) with diffraction plane of (111).

Diffraction peaks due to titanium and copper metal is expected, however, for NT/Cu 90, a low intensity peak at 36.96°

Table 1 Copper dimensions (nm) and Cu in percentage weight (wt%) as determined *via* EDX

Before DPBS	Particle size (nm)	Clusters (nm)	Cu (wt%) before DPBS	Cu (wt%) after DPBS
NT-Control	N/A	N/A	N/A	N/A
Ti/Cu 60	190.65 ± 21.8	3355.00 ± 0.60	57.74 ± 2.69	14.72 ± 6.99
NT/Cu 30	99.87 ± 14.35	323.96 ± 32.97	44.79 ± 1.75	15.06 ± 5.65
NT/Cu 60	61.65 ± 6.6	227.07 ± 22.49	53.47 ± 2.77	30.73 ± 6.07
NT/Cu 90	132.46 ± 11.29	528.57 ± 65	67.27 ± 5.65	59.90 ± 10.10

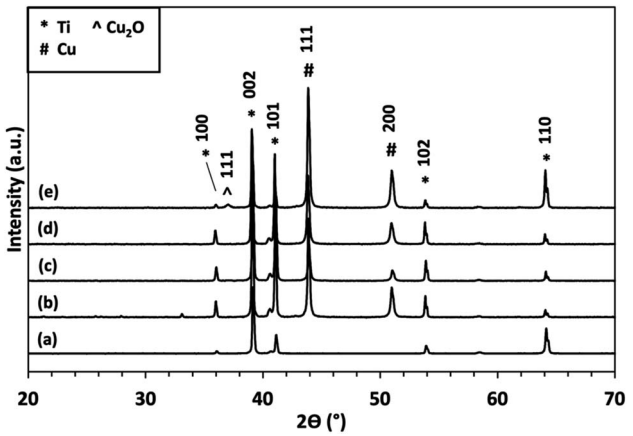

Fig. 3 XRD patterns of (a) NT-Control, (b) Ti/Cu 60, (c) NT/Cu 30, (d) NT/Cu 60, and (e) NT/Cu 90.

denoting the development of the Cu_2O (111) diffraction plane provides an explanation for the observed differences in copper particle morphology compared to NT/Cu 30 and NT/Cu 60. As will be discussed in the following section, the intensity of this Cu_2O (111) peak increases, along with another variation of the copper morphology compared to NT/Cu 30 and NT/Cu 60.

Cu particle formation begins with the electrochemical reduction of the Cu^{2+} ions from the precursor $CuSO_4 \cdot 5H_2O$ salt. Minimisation of hydrogen gas was achieved through the use of AC electrodeposition, so that the premature removal and damage to the arising Cu structures are limited. As the NT sample acts as the cathode, the Cu^{2+} ions from the electrolyte is electrochemically reduced to Cu metal. The way in which the copper particles deposited onto the NT surface varied with electrodeposition time, while there was minimal variation in the copper morphology between electrodeposited Cu on non-NT and NT surfaces (Fig. 1(b) and (d)).

With increasing electrodeposition time, the copper content increased and the propensity for Cu oxidation increased. Lower deposition times (<90 s) resulted in the Cu particles remaining as Cu metal, without a change in the morphology from Ti/Cu 60. For NT/Cu 90, the duration for deposition resulted in a change in the Cu particle morphology and a higher Cu content (Fig. 2 and Table 1). This variation may be influenced by the underlying NT layer and that the increased electrodeposition duration is a result of epitaxial growth. Such a phenomenon was previously reported,[11] in which the Cu morphology could be tended towards tetragonal geometry.

The longer electrodeposition duration of 90 s was also sufficient for the partial oxidation of the electrodeposited Cu to Cu_2O, as observed *via* XRD analysis (Fig. 3). The complete oxidation to CuO was not observed due to the mild experimental conditions used, in particular, a thermal annealing stage was not involved in during immersion of the samples in DPBS.

The surface roughness was carried out and measured in terms of the arithmetic mean deviation (R_a) and the mean height (R_c) (Fig. 5). The average roughness, R_a, provides a means of determining the average deviation of peaks and valleys from the sample mean. The R_a was found to be below 0.6 μm for the nanotubular surfaces, while the non-nanotubular surface (Ti/Cu 60) has a R_a of 1.0 ± 0.1 μm. This implies that the lack of NTs results in a layer of Cu deposits that are rougher than if they were deposited on the NTs. Similarly, the R_c values provide an alternative measure of roughness by comparing the average heights of all major peaks along a sample length. Ti/Cu 60 was found to have a R_c value of 3.90 ± 0.7 μm, which was significantly higher than the NT-Control and the copper-incorporated NT surfaces.

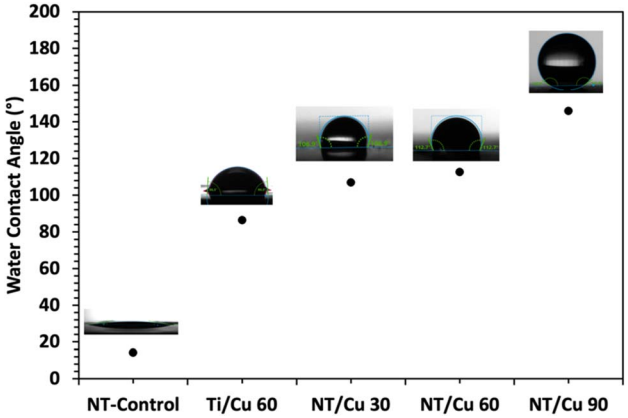

Fig. 5 Water contact angles of control surfaces.

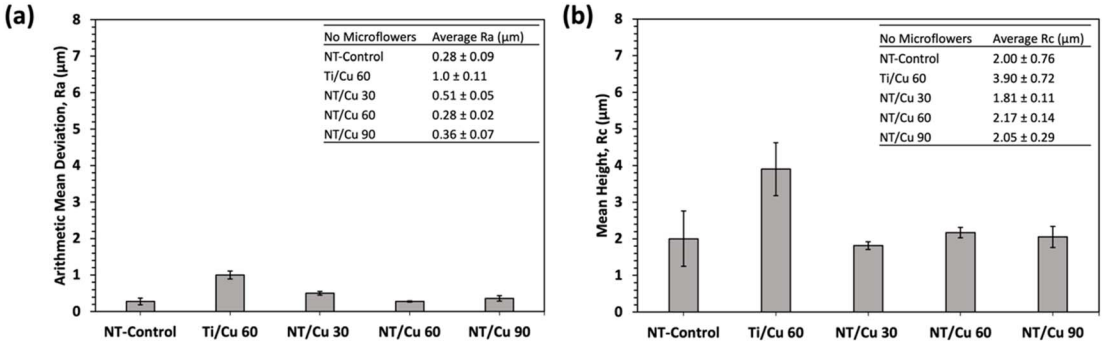

Fig. 4 Surface roughness measurements of NT-Control and the copper-incorporated surfaces after electrodeposition in terms of (a) R_a and (b) R_c.

The surfaces were assessed in terms of wettability, as bacteria tend to prefer to adhere to polar surfaces compared to non-polar surfaces. Following water contact angle measurements, it was found that the NT-Control surface had a contact angle of 14.18°. Upon deposition of the copper particles, the contact angle increased to 86° for Ti/Cu 60, and

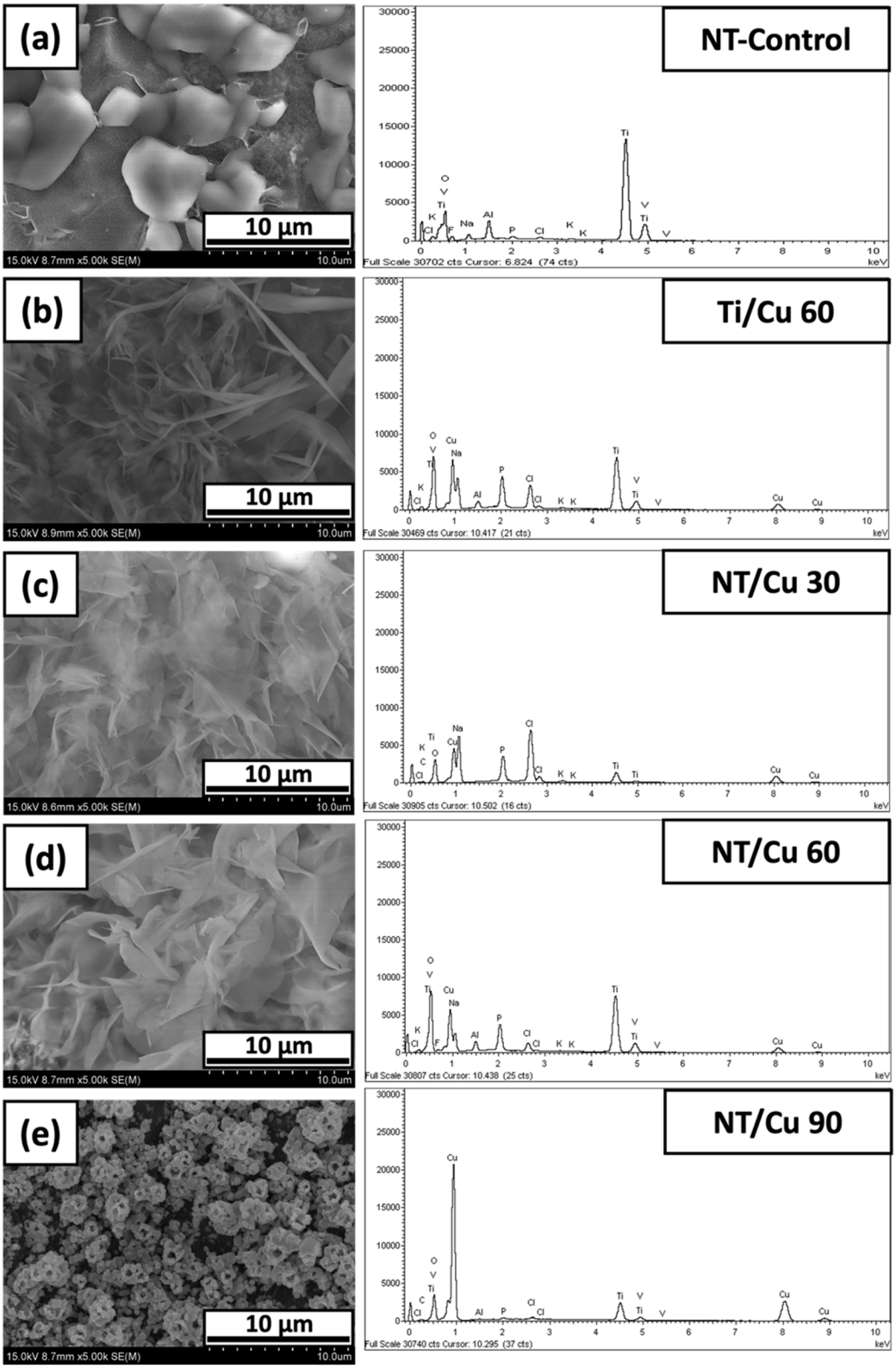

Fig. 6 SEM images and accompanying EDX spectra of (a) NT-Control, (b) Ti/Cu 60, (c) NT/Cu 30, (d) NT/Cu 60, and (e) NT/Cu 90. The surfaces were analysed following immersion in DPBS at 37 °C for 24 hours.

the copper-incorporated NT surfaces resulted in contact angles exceeding 100°.

The NT surfaces are expected to be wettable due to its high aspect ratio structure where the water droplet is further absorbed within the NTs. As copper metal is known to be hydrophobic,[25] it was found that the electrodeposited copper surfaces exhibited increasingly hydrophobic attributes with increasing copper content, which was affected by the duration of electrodeposition. The longest electrodeposition time of 90 s resulted in a contact angle of 146°. This hydrophobicity is typically termed "superhydrophobic" and presents a surface that would be suitable for self-cleaning applications. The difference in morphology between copper particles electrodeposited for 30 and 60 seconds *versus* 90 seconds suggests that the highly dewetting properties of NT/Cu 90 can be attributed to the particle shape and crystallinity, which enhance hydrophobicity.

2.2 Characterisation of Cu-incorporated NTs after immersion in DPBS

2.2.1 Surface morphology and elemental composition. DPBS was employed to analyse the leaching capabilities of the copper particles to release Cu^{2+} ions in a simulated physiological medium that did not contain Ca^{2+} or Mg^{2+} ions. After 24 hours immersion, all Cu-incorporated surfaces, except for NT/Cu 90, had a morphological change from spherical particles to microflowers (Fig. 6). NT/Cu 90 appeared to have retained the clusters with particle diameters of 431 ± 35 nm. Following EDX analysis, the Cu to P ratio was determined, as shown in Table 2. NT/Cu 90 exhibited a much higher Cu atomic% compared to P which suggested that some structural interference was involved to prevent the formation of microflowers as opposed to the other copper surfaces.

There is an overall decrease in the Cu content after immersion in DPBS for all copper-incorporated surfaces, Table 1. A significant decrease in Cu content indicates poor adhesion of the copper particles to the surface. This has implications on the shape of the Cu particles that remain on the surface. Such is noted especially for NT/Cu 90, which did not have a significant decrease in Cu content after immersion in DPBS. The shape of the particles did not morph into the microflowers as seen for the other Cu-incorporated samples, and retained the initial globular morphology and distribution.

The morphology and the attributing crystallinity influence the way in which the copper particles form upon exposure to TSB and DPBS. The morphological and elemental composition of the Cu particles were compared with surfaces that were not exposed to DPBS. The SEM/EDX of the surfaces exposed to only TSB do not exhibit microflower formation (see ESI†). Instead, the copper particle shapes are retained similarly to what was observed in Fig. 1.

2.2.2 Phase composition and Cu^{2+} ion release into DPBS. To further investigate the composition of the microflowers that were formed, XRD analysis was carried out (Fig. 5). The development of microflowers results in additional diffraction peaks that are attributed to the formation of Cu_2O and $Cu_3(PO_4)_2 \cdot 3H_2O$. The disappearance of the copper metal peaks at 44° and 51° are also noted, which contributes to an observed transformation of Cu to Cu_2O. The development of Cu_2O is observed for Ti/Cu 60, NT/Cu 60 and NT/Cu 90 after immersion in DPBS. The Cu_2O (DB card 9005769) diffraction peaks (110), (111), (200), and (220) are observed at 2θ values of 30.13°, 36.96°, 42.83°, and 61.83°, respectively.

The partial oxidation of Cu to Cu_2O as opposed to CuO implies that preferred orientation may be involved in the formation of the $Cu_3(PO_4)_2 \cdot 3H_2O$ microflowers. Considering the deposition of Cu metal before immersion of the surfaces in DPBS, planes (111) and (200) were observed. The (111) diffraction plane for Cu_2O at 2θ 36.96° is developed only for Ti/Cu 60, NT/Cu 60 and NT/Cu 90, which had an initial surface Cu content of 57.74 ± 2.69 wt%, 53.47 ± 2.77 wt%, and 67.27 ± 5.65 wt%, respectively.

At 2θ values below 15°, peaks at 9.74° and 13.47° are observed for all copper-incorporated samples, which are attributed to $Cu_3(PO_4)_2 \cdot 3H_2O$ (JPSCD 00-022-0548). The remaining peaks are attributed to residual NaCl (DB card 9006378: COD) which appear at 32.22° and 45.92°. Due to the maintenance of surface copper concentration as determined *via* EDX analysis, the formation of polyhedral particles on top of other Cu particles is shown in the SEM images. Following analysis of the copper phase *via* XRD, the formation of Cu_2O was determined with diffraction planes (110), (111), (200), and (220) at 2θ values of 30.13°, 36.96°, 42.83°, and 61.83°, respectively.

The development of diffraction peaks particularly at 9.74° (200) and 13.47° (110) are attributed to $Cu_3(PO_4)_2 \cdot 3H_2O$, which are present for all copper surfaces. Along with the disappearance of the (111) and (200) Cu metal diffraction planes, all Cu particles were converted to $Cu_3(PO_4)_2 \cdot 3H_2O$ microflowers. In the case of NT/Cu 90, where there was an excess of Cu, there was also a noted increase in intensity of the (111) Cu_2O plane. The development of the remaining (110), (200), and (220) Cu_2O planes further support the fact that preferred growth of the polyhedral copper particles is attributed to the initial development of the (111) plane. Such a development has been previously reported for Cu_2O, where generation of a particular

Table 2 $Cu_3(PO_4)_2 \cdot 3H_2O$ microflower dimensions (nm) and Cu in percentage weight (wt%), Cu : P atomic ratio, and Cu^{2+} ion released in DPBS

After DPBS	Plate thickness (nm)	Clusters (nm)	Cu : P	Cu^{2+} ions released (ppb)
NT-Control	N/A	N/A	N/A	N/A
Ti/Cu 60	125.08 ± 30.00	N/A	4.18	138.53 ± 26.73
NT/Cu 30	116.32 ± 39.48	N/A	4.23	84.53 ± 8.57
NT/Cu 60	118.71 ± 19.06	N/A	3.23	122.52 ± 19.23
NT/Cu 90	N/A	567.57 ± 71.47	84.37	161.11 ± 90.68

exposed facet of Cu_2O is principally responsible for the morphology that the Cu particles can adopt.[6] The development of the (111) Cu_2O is also noted for Ti/Cu 60 and NT/Cu 60.

The oxidation of Cu films to other copper oxides is reported by Choudhary *et al.*,[6] where a similar evolution of XRD peaks due to CuO/Cu_2O formation is observed, and highly dependent on oxygen content and elevated temperatures. The development of such peaks coincides with the dramatic change in the Cu morphology, and it is suspected that due to the higher duration of Cu loading, this would result in the deposition of copper at preferred areas and so growth along a preferred plane may explain why NT/Cu 90 is different in shape and phase compared to the rest of the copper-incorporated samples.

The surfaces that formed microflowers were found to be highly ordered and appeared to grow in one direction. As observed at 9° and 13° in the XRD patterns, the microflowers were attributed to the formation of $Cu_3(PO_4)_2 \cdot 3H_2O$.[26,27] While reports show nanoflowers consisting of $Cu_3(PO_4)_2 \cdot 3H_2O$, the experimental conditions and the resulting XRD patterns match those observed for the morphology change for the Cu-incorporated nanotube samples. The reported synthesis route of nanoflowers involved the incubation of a suspension of 120 mM of $CuSO_4$, PBS solution, and a source of amine groups, such as dopamine or proteins.[4] After the required time had passed, nanoflowers would self-assemble in the suspension. Flowers for the current work can only be observed in the micrometer scale with sizes 19 ± 4 μm, 41 ± 9 μm, and 34 ± 4 μm for Ti/Cu 60, NT/Cu 30 and NT/Cu 60, respectively, and it appears that the underlying absence of a TiO_2 NT layer results in smaller microflowers compared to the presence of the NT layer.

Following characterisation of the copper deposits on the NT surface through changes in the shape, elemental composition and crystallinity, the extent at which the copper-incorporated samples release Cu^{2+} ions was assessed *via* ICP-OES measurements. Considering the presence of Cu_2O after DPBS immersion, it is expected that a related concentration of Cu^{2+} ions were released into the surrounding DPBS medium. With increasing electrodeposition times, the amount of surface Cu increased, along with an increase in the distribution of copper particles. It would then follow that there would be an increase in the concentration of copper leachates, which was observed after 24 hour immersion in Table 2.

The R_a values of the surfaces following DPBS exposure did not significantly change for Ti/Cu 60 and NT/Cu 30, however, the overall roughness of the NT-Control, NT/Cu 60 and NT/Cu 90 significantly increased. The R_c values were increased only for NT/Cu 30 and NT/Cu 90.

After exposure to DPBS, the water contact angle for NT-Control increased to 27°, which is likely attributed to deposition of salts onto the NT surface. Surfaces Ti/Cu 60, NT/Cu 30 and NT/Cu 60 all reduced in water contact angle to below 90°, which classifies these surfaces as hydrophilic. This is particularly interesting as the formation of the microflowers only occurs on these surfaces, which were previously hydrophobic due to high copper content. The copper content decreased as the Cu particles transformed to the $Cu_3(PO_4)_2 \cdot 3H_2O$ microflowers (Table 2). The wettability for NT/Cu 90 decreased after

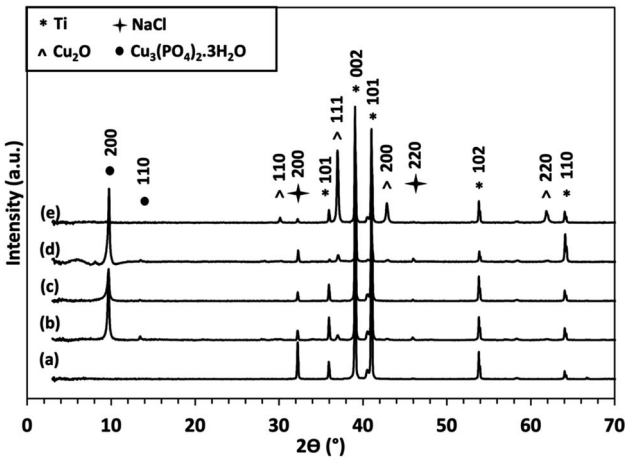

Fig. 7 XRD patterns of (a) NT-Control, (b) Ti/Cu 60, (c) NT/Cu 30, (d) NT/Cu 60, and (e) NT/Cu 90 after immersion in DPBS at 37 °C for 24 hours.

24 hours DPBS immersion. While microflowers do not form on this surface, the change towards hydrophilicity is attributed to the morphological change from large, polyhedral particles with diameters of 132.5 ± 11.3 nm, to larger, irregularly shaped particles with diameters of 431 ± 34.7 nm. The larger copper particles appear to arrange in a way that leave pores between them, and may also contribute to a decrease in the contact angles. This morphological change may also be affected by epitaxial growth, as observed by the highest intensity peak at 38° along the (111) plane in Fig. 7(e). This preferential growth appears to hinder the formation of microflowers, which crystallise along the (200) plane.

In summary, the mechanism at which the microflowers form follows similar aspects as observed for other instances of $Cu_3(PO_4)_2 \cdot 3H_2O$ microflower formation.[28–31] The pH of DPBS remains at 7.2 during and after exposing the copper-incorporated surfaces to the medium. As phosphates are pH-sensitive,[32] the equilibrium that is established involves the dissociation of $H_2PO_4^-$ at pH 7 (reaction (1)).

$$H_2PO_4^- \leftrightarrow HPO_4^{2-} + H^+ \quad (1)$$

Both $H_2PO_4^-$ and HPO_4^{2-} species are present in solution, with HPO_4^{2-} being present in higher concentrations as the pH increases, resulting in further dissociation to yield PO_4^{3-} ions (reaction (2)).

$$HPO_4^{2-} \rightarrow PO_4^{3-} + H^+ \quad (2)$$

A pH gradient develops with the growth the TiO_2 NTs during anodisation.[33] The pH is higher at the bottom of the NTs, resulting in a higher concentration of H^+ ions at the metal oxide/metal interface. The pH increases approaching the metal oxide/electrolyte interface, which is attributed to the increase in OH^- ions.[33]

This increase in OH^- ion concentration contributes towards the negative charge of the NT layer, particularly at NT surface, which electrostatically attract Cu^{2+} ions from the electrolyte to the

NT layer during electrodeposition. The electrodeposition potential of 5 V is sufficient in reducing the Cu^{2+} ions to Cu metal particles, which are influenced by the underlying NT morphology. The electrodeposition potential and duration influence the Cu particle morphology, where potentials higher than 5 V and electrodeposition times exceeding 90 s results in the detachment of Cu particles as well as delamination of the NT layer.

Considering only the effect of electrodeposition time, physical properties such as the morphology, elemental composition and crystallinity affect how the Cu particles interact with the phosphate ions in the DPBS solution. Lower copper content due to low electrodeposition times result in the formation of $Cu_3(PO_4)_2 \cdot 3H_2O$ microflowers, along with a release of Cu^{2+} ions in the range 84 to 122 ppb. Under suitable temperature and pH, the nucleation of the microflowers is initiated by the reaction of PO_4^{3-} ions with the Cu^{2+} ions that are spontaneously formed from the copper particles when immersed in DPBS.[28,31] The microflowers self-assemble from the nucleation sites and are proposed to anisotropically grow[31] along the $Cu_3(PO_4)_2 \cdot 3H_2O$ (200) plane (Fig. 7). Simple mixing of the Cu^{2+} and PO_4^{3-} species is not sufficient for the formation of the microflowers, and it is proposed that a limit of 122 ppb Cu^{2+} ions that are steadily released from the copper-incorporated surfaces is required for microflower formation. The amount of Cu^{2+} ions that is leached is related to the copper content, which can be controlled by the duration of the electrodeposition process (Table 2).

As for longer electrodeposition times such as for NT/Cu 90, a delayed mechanism towards microflower formation is observed. Exposing NT/Cu 90 to DPBS for 24 hours is not sufficient in forming the microflowers, which is due to a combination of high copper content, difference in copper particle morphology, and hydrophobicity results in lower surface area for reaction with PO_4^{3-} ions. However, after 5 days immersion in DPBS, the copper particles transform to $Cu_3(PO_4)_2 \cdot 3H_2O$ microflowers which are complemented by a decrease in Cu content and an increase in surface hydrophilicity (see ESI†).

2.3 Antibacterial activity

Following characterisation of the surface morphology, the antibacterial effect of the presence of Cu_2O as well as the $Cu_3(PO_4)_2 \cdot 3H_2O$ microflowers was investigated against *E. coli* and *S. aureus*, which are two common bacterial strains responsible for IAIs.[34,35]

Antibacterial activity of the copper-incorporated surfaces after immersion in DPBS was observed with p values of at least $p < 0.05$ across the copper samples compared to NT-Control. The NT-Control resulted in log(CFU mL^{-1}) bacterial growth of 9.06 $\pm$ 0.66 against *E. coli* and 6.67 $\pm$ 0.25 against *S. aureus.* To show that the formation of the microflowers conferred 100% inhibition against both bacteria, the NT-Control and Cu-incorporated surfaces were inoculated with the same bacteria in TSB but without the addition of DPBS.

As shown in Fig. 10(a) and (b), bacterial growth varied for the different copper surfaces without DPBS, but none of which performed as well as the microflower-containing surfaces Fig. 10(c) and (d). Ti/Cu 60 samples induced significantly more *E. coli* inhibition compared to NT-Control. There was no significant difference between NT-Control and the other NT/Cu surfaces. In contrast, there were observable differences in the antibacterial activity between NT-Control and copper-incorporated surfaces when exposed to *S. aureus.* A significant decrease in bacterial growth against NT-Control is observed for surfaces NT/Cu 30 and NT/Cu 90 with $p < 0.01$ and $p < 0.05$, respectively.

In this work, it was found that the diameters of the surface-bound copper particles ranged from 60 to 100 nm prior to DPBS exposure. While this resulted in poor antibacterial activity compared to the transformed $Cu_3(PO_4)_2 \cdot 3H_2O$ microflowers (Table 3), there was some evidence of bacterial inhibition. By immersing the samples in DPBS and the bacterium inoculum, the formation of microflowers on site resulted in a 100% inhibition of both bacterial strains. This is postulated to be due to the change in the copper particle morphology to copper-phosphate microflowers, as well as the release of Cu^{2+} ions.

In order to investigate if the combination of microflower morphology and Cu^{2+} ion release was necessary for bacterial inhibition, the electrodeposited surfaces were immersed in DPBS for 24 hours prior to bacterial inoculation. By comparing only the bactericidal effect of as-electrodeposited copper particles against the pre-formed microflowers, it was found that the microflower structure alone was not sufficient to inhibit the bacteria to the same extent as the microflowers formed during bacterial inoculation.

Additional physical characterisation information including the morphological, elemental and phase composition are shown in the ESI.†

2.3.1 Direct bacteria–surface interactions. For the time-varied copper surfaces, it was observed that differences in

Table 3 Summary of all copper-incorporated surfaces where bacterial susceptibility tests were assessed against *E. coli* and *S. aureus*. TNTC refers to bacterial colonies that were too numerous to count

	Log(CFU mL^{-1}) *vs. E. coli*			Log(CFU mL^{-1}) *vs. S. aureus*		
	No microflowers	Microflowers formed during inoculation	Pre-formed microflowers	No microflowers	Microflowers formed during inoculation	Pre-formed microflowers
NT-Control	8.18 $\pm$ 0.73	9.06 $\pm$ 0.66	9.44 $\pm$ 0.08	9.23 $\pm$ 0.16	6.67 $\pm$ 0.25	9.11 $\pm$ 0.22
Ti/Cu 60	3.77 $\pm$ 0.29	0.00	0.00	8.40 $\pm$ 1.19	0.00	0.00
NT/Cu 30	6.96 $\pm$ 0.98	0.00	TNTC	6.31 $\pm$ 0.32	0.00	0.00
NT/Cu 60	8.75 $\pm$ 0.35	0.00	5.39 $\pm$ 0.16	8.21 $\pm$ 0.43	0.00	3.58 $\pm$ 0.00
NT/Cu 90	7.21 $\pm$ 0.41	0.00	4.37 $\pm$ 0.21	7.63 $\pm$ 1.01	0.00	3.60 $\pm$ 0.00

surface morphology influenced the antibacterial properties of copper-incorporated surfaces. Specifically, samples Ti/Cu 60, NT/Cu 30, and NT/Cu 60 exhibited microflower formation, whereas NT/Cu 90 did not. Antibacterial tests were conducted to examine if there is a relationship between the morphology of the copper deposits and their ability to inhibit bacterial growth.

While the exact mechanisms at which copper in particular remains a debated topic, the following attempts to consider how the physical properties of the copper-incorporated surfaces directly contribute towards the observed antibacterial activities. This can be considered in terms of surface morphology, roughness, and hydrophilicity/hydrophobicity.[10]

The antibacterial effectiveness of the copper-incorporated nanotubes (NTs) was tested against *E. coli* and *S. aureus*. Results showed that the NT/Cu surfaces did not significantly affect *E. coli* growth compared to the NT-Control. This can be attributed to the inherent membrane elasticity of Gram-negative bacteria like *E. coli*, which may provide resistance to copper-induced stress. Additionally, studies have shown that *E. coli* can upregulate efflux pump proteins, such as those encoded by the copA gene, to extrude copper particles from the cell cytosol to the periplasm upon exposure to heavy metals.[36] Other proteins, like CueO, help reduce toxicity by converting Cu^{+} ions to the less toxic Cu^{2+} ions.[37]

In contrast, for *S. aureus*, the NT/Cu 90 surface significantly decreased bacterial growth compared to NT-Control. NT/Cu 90, characterised by its globular copper deposits and the absence of microflowers, showed the highest concentration of leached Cu^{2+} ions after 24 hours (161.11 ± 90.7 ppb). This sample also exhibited superhydrophobicity, indicated by a water contact angle of 146°, which corresponds with a high copper content (59.9 ± 10 wt%). The hydrophobic nature is further enhanced by the presence of Cu_2O, a compound known for its inherent hydrophobic properties.[38]

The superhydrophobic behaviour of the NT/Cu 90 surface is linked to the hierarchical nano/microstructures that develop over longer electrodeposition times, as reported for various Cu_2O-based structures.[38,39] As described by the Cassie–Baxter model, the trapped air within these copper particle structures reduces the contact area between water and the surface, resulting in a surface that is not fully wet.[40,41] Over longer deposition times, more copper is deposited on the NT surface, but the outermost copper layers, which are less tightly adhered to the substrate, are more prone to oxidation. Prior to DPBS exposure, NT/Cu 90 develops Cu_2O (Fig. 3(e)). The combination of the surface shape (Fig. 2(d)), the Cu content (Table 1), surface roughness (Fig. 4), and the presence of Cu_2O contribute towards the surface superhydrophobicity.

Following DBPS exposure, NT/Cu 90 transitions from a superhydrophobic surface to a hydrophobic surface that is better described as being in the Wenzel state.[41] This is attributed to the complementary change in the surface morphology and the leaching of Cu^{2+} ions.

The role of chloride ions in shaping the copper structures was also considered. Chloride ions are known to adsorb selectively along specific crystal planes, influencing the growth of deposited copper.[42] For NT/Cu 90, the (200) NaCl plane may influence $Cu_3(PO_4)_2 \cdot 3H_2O$ growth along the (200) plane, as well as the reduced copper deposition due to the shorter electrodeposition time. Interestingly, NT/Cu 60 exhibited the highest Cl content (0.55 ± 0.14 wt%), which corresponded to the highest phosphorus content (9.50 wt%). This suggests that high Cl concentrations may not always favour ordered microflower formation and might instead promote the formation of both copper(II) phosphate and copper(I) oxide. It is also considered that the role of chloride ions may be involved in mediating the release of Cu^{2+} ions, which may affect the self-assembly of the microflowers.

Two mechanisms are at work when the bacteria interact with the copper-incorporated surfaces. For surfaces Ti/Cu 60, NT/Cu 30 and NT/Cu 60, the first interaction involves the phase transformation from the copper metal to the $Cu_3(PO_4)_2 \cdot 3H_2O$ microflowers. The added surface roughness provided by the copper deposits would disrupt the bacterial attachment.[10] While microflowers did not form for NT/Cu 90, the transformation to Cu_2O particles exhibits some antibacterial activity by making the surface superhydrophobic due to the increased Cu content and the hydrophobic Cu_2O. The physical aspects of the microflowers, along with the nano-roughness (Fig. 8) afforded by the NTs to minimise bacterial cell membrane attachment, complement the overarching active-contact mechanism in which the developing microflowers exert bactericidal activity through direct contact killing.

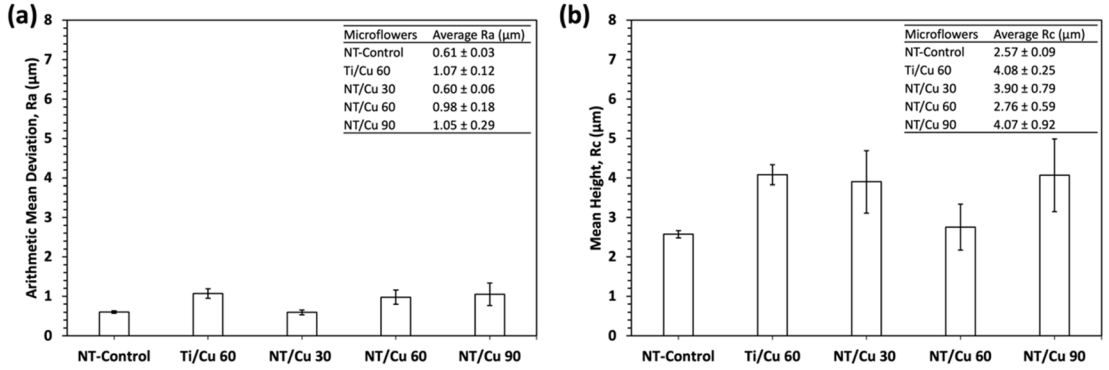

Fig. 8 Surface roughness measurements of surfaces following DPBS exposure in terms of (a) R_a and (b) R_c.

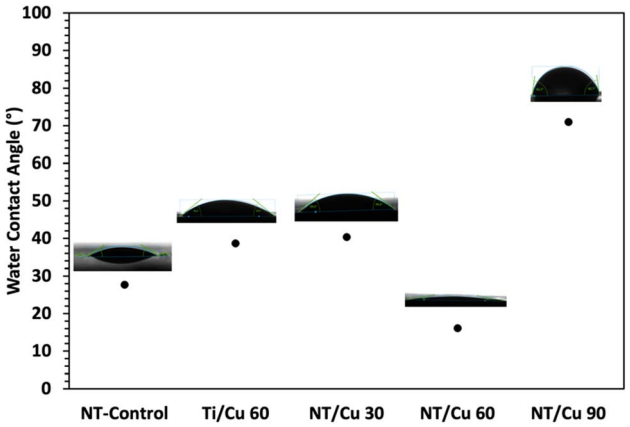

Fig. 9 Water contact angle of surfaces following DPBS exposure.

Following exposure to DPBS, the microflowers begin to exhibit hydrophilic behaviour (Fig. 9). This follows from the initially hydrophobic behaviour of the copper surfaces which suggests that the initial antibacterial stage of adhesion is abated by the hydrophobicity. Overtime, as the hydrophobic nature of the copper-incorporated NT surfaces shifts to hydrophilicity, a difference in the interaction between the surfaces and the bacteria may arise, and an alternative mechanism for bacterial inhibition is observed, such as the development of a dense hydration layer which results in an increase in energy for bacteria to adhere to the surface.[43]

The second way in which the copper-incorporated surfaces function when introduced to the bacteria is through the release of Cu^{2+} ions into the surrounding media. As phosphates can be considered as chelating agents,[44] the amount of Cu^{2+} ions that are released from the surface are limited by the amount of copper available to bind with phosphate ions in solutions. Due to the absence of a NT layer for Ti/Cu 60, 139 $\pm$ 27 ppb of Cu^{2+} ions were leached. This is comparable to NT/Cu 90, which yielded 161 $\pm$ 91 ppb Cu^{2+} ions. Even though a phase transformation was observed for Ti/Cu 60, the sudden escalation of Cu^{2+} ions released is attributed to the poor adhesion of the

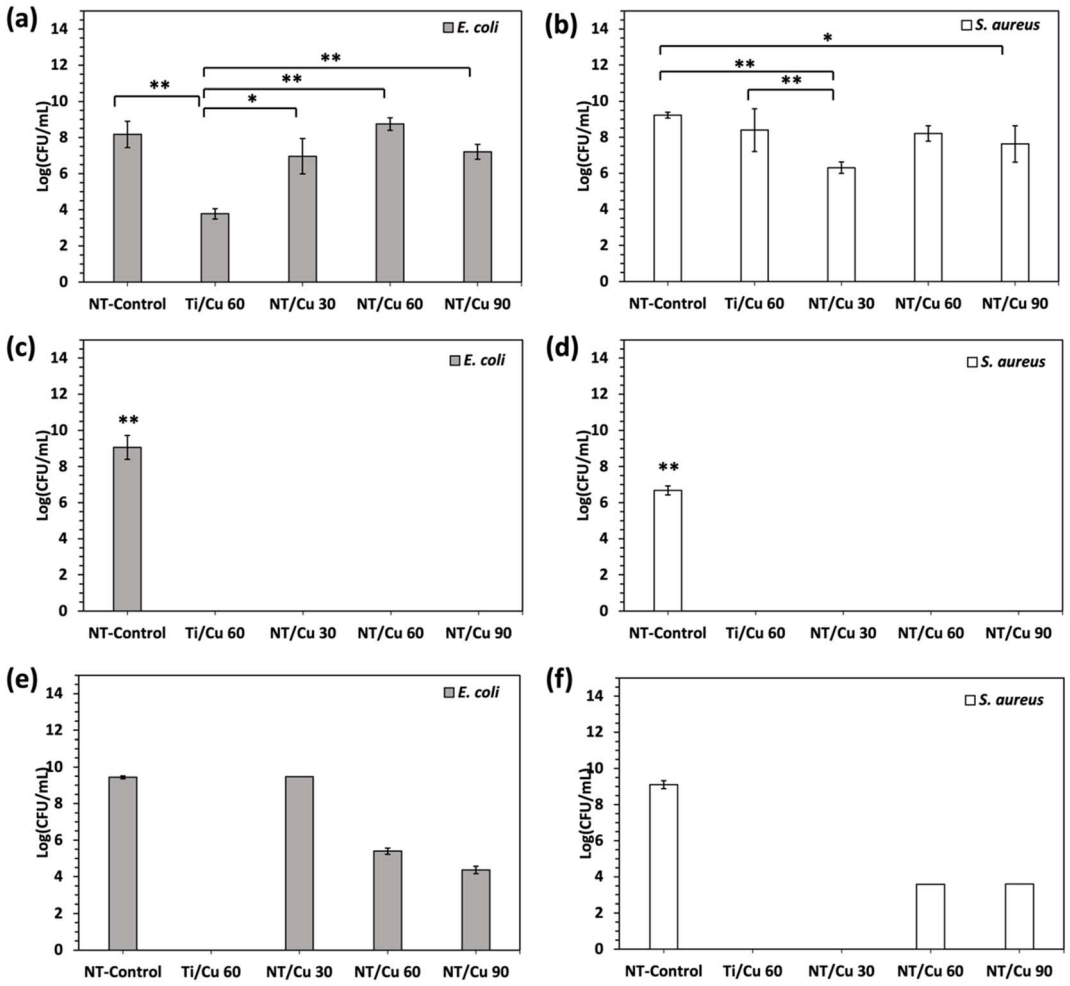

Fig. 10 Number of viable colonies in the countable range 30–300 colonies are reported as log(CFU mL^{-1}) for copper-incorporated NTs that were electrodeposited at 5 V for 30 s, 60 s, and 90 s against *E.coli* and *S. aureus*. Surfaces that were only exposed to TSB and did not form microflowers are shown in (a) and (b). Surfaces that formed microflowers during inoculation are shown in (c) and (d) with 100% bacterial inhibition. Surfaces that were pre-treated with DPBS prior to inoculation are shown in (e) and (f). Error bars represent 95% confidence interval. *Represents $p < 0.05$ significance and **represents $p < 0.01$ significance, as determined using one-way ANOVA and *post hoc* Tukey–Kramer tests.

copper particles to the bare Ti surface. As for NT/Cu 90, despite the enhanced adhesion due to the NT layer, the formation of Cu_2O resulted in a high concentration of leachates, as Cu_2O is known to be highly soluble in aqueous media.[45] The presence of chelating species would influence the extent of bactericidal activity.[46] The different bacterial interaction is attributed to the antibacterial activity observed for NT/Cu 90. The 100% antibacterial rate is due to the change in the morphology, the added formation of Cu_2O, as well as the comparable leaching of Cu^{2+} ions to Ti/Cu 60.

To determine the antibacterial activity of the electrodeposited surfaces in terms of passive and active coatings, a combination of EDX, XRD, and ICP-OES was used. Passive coatings prevent initial bacterial attachment, and are preferred for long-term treatment.[12,43] Following 24 hour immersion of the electrodeposited samples, XRD was carried out to verify any oxidation products that have remained on the surface (Fig. 7). Considering how Cu^{2+} ions are released from the surface, it is of interest to check if the remaining copper oxides are present, and whether the oxides would contribute towards direct-contact bactericidal activity.

Active antibacterial functions would involve consideration of the antibacterial material for retention of the antibacterial effect at a sustained level, where not only the origin of the antibacterial agent deposition method is considered, but also the rate at which such agents are released from the surface. This considers multiple effects such as the nanomorphology of the TiO_2 NT layer as well as the influence of such structures have on the copper that is deposited either on top of the layer or within the layer. In general, active antibacterial activity involves the sustained release of an antibacterial agent over an extended period of time, or for however long the biomedical part is required. Active behavioural characteristics would also have to take into account the surrounding media, or local effects, and ensuring an antibacterial environment that avoids the evolution of a local bacterial infection to the otherwise fatal systemic infection, which is typically through hematopoietic spread.[35,47]

2.3.2 The effect of Cu^{2+} ion release. Antibacterial activity tests resulted in 100% inhibition against *E. coli* and *S. aureus* after 24 hours exposure. This bacteriostatic result is only observed for surfaces that have formed the microflowers in the presence of DPBS, and have leached a quantity of Cu^{2+} ions during microflower formation.

Most reports that investigate the effect of copper as antibacterial surfaces preliminarily involve the use of pure copper, which are thermally annealed to form Cu_2O, CuO, or a composite of the two oxides.[7] According to such reports, direct metal contact killing was considered the principal mode at which antibacterial activity is exerted. Investigations into whether the level of Cu^{2+} ions are affected by the media that the surfaces are exposed to were carried out by Molteni *et al.*[45] In addition, the extent at which Cu_2O or CuO contribute to bactericidal activity was carried out by Hans *et al.*[48] The authors hypothesised that the extent of copper corrosion may contribute to direct contact killing in the form of Cu^{+} or Cu^{2+} ions being released during copper corrosion. In both of the above cases, it was noted that agents which are known to complex copper were used, namely Tris, Tris-Cl and phosphate-based media such as phosphate buffer. The complexing of Cu would affect the amount of Cu^{2+} available in solution and affect the amount of Cu^{2+} that may be extruded from the bacteria.

Despite the enhanced antibacterial behaviour afforded by the increased Cu^{2+} ions released from Ti/Cu 60 samples, it may pose adverse effects in terms of re-infection after the initial inhibition stage. Various mechanisms of action of copper antibacterial agents have been proposed, and it is well-accepted that the initial stage of inhibition involves direct contact killing,[7,10] followed by membrane disruption and/or the incorporation of Cu species in the bacterium cell to induce formation of reactive oxygen species. The *in situ* transformation of copper particles with various morphologies, and for the species that has retained a <60 wt% Cu, to the $Cu_3(PO_4)_2 \cdot 3H_2O$ microflowers introduced an added bacterial–surface interaction that supplemented bactericidal Cu^{2+} ion leaching activity. The highest amount of Cu^{2+} ions leached from the surfaces investigated in this work was 161 ± 91 ppb (2.5 ± 1.4 μM), which is far lower than the minimum inhibitory concentration (MIC) values obtained for Cu^{2+} ions released from copper-containing surfaces, which were reported to be 448 ppb against *S. aureus* and 256 ppb against *E. coli*.[49] This is promising considering that the electrodeposited face that was exposed for electrodeposition was 1 cm^2. The Cu^{2+} ion concentrations released into DPBS (Table 2) resulted in 100% antibacterial activity also provides promising implications in terms of enhanced biocompatibility. Cytotoxicity levels of copper without compromising MC3T3 osteoblast viability is 9000 ppb.[50] The current work provides a potential route to combine a range of mechanisms that are accepted as Cu bactericidal strategies. Namely, the combination of nanorough surfaces afforded by the NTs confer changes in the electrodeposited Cu particle morphologies. The Cu shapes after exposure to DPBS influences the extent of Cu^{2+} ion leaching, and the work further attributes the observed antibacterial activity due to the complementary changes in copper crystallinity, copper content, microflower formation, and hydrophobicity.

3. Experimental

3.1 Materials and methods

Ti6Al4V sheets (1 mm thickness; titanium grade 5, SAS Titanium Services, France) were cut into 2.5 cm × 2.5 cm panels. Ammonium sulphate, ammonium fluoride, hydrofluoric acid, nitric acid, sulfuric acid, and copper(II) sulphate pentahydrate were purchased from Sigma Aldrich and used without further purification. The NT sample was placed in a flat specimen holder (25 × 25 mm, Redoxme AB) with a circular area of 1 cm^2 (single face) exposed to the electrolyte. The electrolyte used for copper electrodeposition was composed of copper(II) sulphate pentahydrate (1 M), sulfuric acid (1% v/v), and deionised water. Microbiological experiments involved the use of tryptic soy broth (TSB), maximum recovery diluent (MRD), and plate count agar, which were purchased from Scharlab.

Anodisation experiments were performed using a power supply (HMC 8043 Ronde & Schwarz) attached to a digital multimeter (HMC 8012 Ronde & Schwarz). The temperature of the

two-electrode cell was maintained at 17 ± 1 °C by use of a recirculation bath. The anodised titanium panels served as the anode and they were held by a titanium jig. A panel of stainless steel (304) served as the cathode. The electrolyte solution was agitated by air. To observe the copper particles within the NTs, Cross Hatch Adhesion Tape (ASTM D3359-22, Elcometer 99) was applied for 2 minutes and carefully removed immediately before SEM analysis.

Electrodeposition experiments were performed using an alternating current (AC) power supply (12 V variable Electrosound). The experiments were carried out in a two-electrode cell, where the anodised titanium sample served as the cathode, and a copper plate was used as the anode. The NT sample was placed in a flat specimen holder (2.5 × 2.5 cm, Redoxme AB) with a circular area of 1 cm^2 (single face) exposed to the electrolyte. The electrolyte solution was magnetically stirred, and experiments were carried out at room temperature.

3.2 Preparation of a TiO_2 nanotubular surface *via* anodisation

Prior to anodisation, the titanium panels were ultrasonicated in acetone for 5 minutes, followed by ultrasonication in isopropanol for another 5 minutes. The pickling pre-treatment involved immersion of the titanium sample in a solution of HF (2% w/w) and HNO_3 (37% w/w) which was magnetically stirred, at room temperature. The sample was rinsed in two 5 minute sessions with deionised water.

The titanium samples were subsequently anodised in an electrolyte solution consisting of ammonium sulphate (1 M) and ammonium fluoride (0.25 M) for 30 minutes at an applied voltage of 20 V. Following anodisation, the anodised surfaces were rinsed in two 5 minute session of deionised water and dried in air.

3.3 Preparation of the copper-incorporated surface

Copper electrodeposition experiments were carried out in a two-electrode cell where the TiO_2 NT served as the cathode and a copper plate served as the anode. Following AC electrodeposition, the samples were rinsed with deionised water for 2 minutes and dried. Ti/Cu 60 represents a non-anodised surface that was electrodeposited with copper at an applied voltage of 5 V for 60 seconds. NT/Cu 30, NT/Cu 60 and NT/Cu 90 denote anodised surfaces that were electrodeposited at an applied voltage of 5 V for 30 s, 60 s, and 90 s, respectively.

3.4 Surface characterisation

3.4.1 FE-SEM/EDX. Surface characterisation, including topography, morphology and particle size, was obtained using field-emission scanning electron microscopy (FE-SEM) (Hitachi SU-70) at an accelerating voltage of 10–15 kV. To analyse the surface morphology and cross-sections, the samples were coated with a 4 nm layer of Pt/Pd (Cressington 208HR Sputter coater) prior to imaging. Energy-dispersive X-ray (EDX) analysis (Oxford Instruments 50 mm^2) was carried out at an accelerating voltage of 15 kV. Prior to analysis, the samples were coated with a 15 nm layer of carbon (Cressington 208C Carbon Coater).

3.4.2 XRD. X-ray diffraction (XRD) analysis (Rigaku MiniFlex 600) was carried out using Cu-K_α radiation at 40 kV and 15 mA in the range 3° to 90° (2θ) with speed 5° min^{-1} at a step of 0.01° (2θ) and the analysis was carried out using the associated software (SmartLab Studio II).

3.4.3 Surface roughness and water contact angle. Surface roughness measurements were carried out using the Surfcom 130A (Accretech). The evaluation length was set at 5 mm, and allowed to scan at a speed of 0.3 mm s^{-1}, at three different sites per sample ($n = 3$). The Mobile Surface Analyser (Kruss) was used to perform water contact angle measurements. The associated software was used to measure the contact angle of a 1 μL water droplet at three different sites per sample ($n = 3$).

3.4.4 Long-term immersion tests in DPBS. In order to determine the concentration of metal ions released into the surrounding media, the samples were immersed in DPBS at 37 °C over 24 hours. The concentrations of released Cu^{2+} ions were analysed *via* inductively-coupled plasma optical emission spectroscopy (ICP-OES, Vista-PRO CCD Simultaneous ICP-OES). Standards using the ICP multi-element standard solution IV (1000 mg L^{-1}) were diluted into concentrations of 200, 400, 600, 800, 1000, 1200 and 1500 ppb. These standards were used to establish a calibration plot for Cu concentration prior to analysis. Data analysis was performed using the associated software (Varian ICP expert, version 4.1.0).

3.5 Antibacterial properties *via* colony forming unit (CFU) count

Escherichia coli (ATCC 25922 Microbiologics) and *Staphylococcus aureus* (ATCC 25923 Microbiologics) were used for the following microbiological experiments. Prior to use, the bacteria were inoculated in 10 mL tryptic soy broth (TSB) and incubated at 37 °C for 24 hours.

To assess the antibacterial activity of the copper-incorporated surfaces, ISO 22196 for antimicrobial testing of antimicrobial surfaces was adapted for metal surfaces. The sample surfaces were autoclaved and 100 μL of DPBS was added, followed by inoculation with 100 μL of bacterial suspension adjusted to a concentration of 1×10^6 CFU mL^{-1} (McFarland value 0.5). The samples were incubated at 37 °C over 24 hours.

The test samples were then transferred into a stomacher bag containing 9 mL of maximum recovery diluent (Scharlau). Six 1 in 10 serial dilutions of the sample bacterial solution were performed and subsequently plated on agar plates, which were incubated at 37 °C for 24 hours. The resulting bacterial colonies were counted and the antibacterial rate was calculated with respect to the control sample (NT-Control). All experiments were done in triplicate, $n = 3$. Countable colonies within the range 30–300 colonies were included for data analysis.

4. Conclusions

The current work presents an electrochemical method utilising the TiO_2 NT morphology afforded by anodisation of titanium for subsequent development of an antibacterial surface. The TiO_2 NTs were modified to allow for the electrodeposition of copper, in

which the shape that the deposited copper particles adopt is principally affected by the duration of the electrodeposition process. Microflowers consisting of $Cu_3(PO_4)_2 \cdot 3H_2O$ are formed on the NT surface following an applied voltage of 5 V for a maximum duration of 60 s, and immersion in DPBS for 24 hours. The initial morphology, copper content, and crystallinity of the copper deposits directly affects the concentration of Cu^{2+} ions that are released. The physical characteristics of the initial deposits influence the development of $Cu_3(PO_4)_2 \cdot 3H_2O$ microflowers. It is proposed that a combination of the microflower morphology and the release of Cu^{2+} ions directly influence the antibacterial activity against *E. coli* and *S. aureus*. Future work is needed to investigate the long-term antibacterial effects of the microflowers and the necessary biocompatibility tests to assess cytotoxicity and cell viability.

Data availability

All data can be found within this manuscript and in the ESI.†

Author contributions

Justynne Fabian: analysis, writing, experimental, characterisation, Grant Morton: ICP-OES, Shubham Sharma: microbiology supervision and troubleshooting, Brendan Duffy: supervision and review, Susan Warren: supervision and review.

Conflicts of interest

There are no conflicts of interest to declare.

Acknowledgements

This publication has emanated from research conducted with the financial support of Taighde Éireann – Research Ireland under Grant number [GOIPG/2022/2095]. I would also like to acknowledge the support provided by the Centre for Research in Engineering Surface Technology (CREST), the Physical to Life Sciences Research Hub, and the Sustainability and Health Research Hub (SHRH) for the provision of analytical instruments and microbiology facilities.

References

1 Z. Pan, C. Dai and W. Li, *Biochem. Biophys. Rep.*, 2024, **39**, 101764, DOI: **10.1016/j.bbrep.2024.101764**.
2 Z. Yuan, Y. He, C. Lin, P. Liu and K. Cai, *J. Mater. Sci. Technol.*, 2021, **78**, 51–67, DOI: **10.1016/j.jmst.2020.06.074**.
3 J. Dong, W. Wang, W. Zhou, S. Zhang, M. Li, N. Li, G. Pan, X. Zhang, J. Bai and C. Zhu, *Biomater. Res.*, 2022, **26**, 1–33, DOI: **10.1186/s40824-021-00262-8**.
4 X. Zhang, Z. Zhang, Q. Shu, C. Xu, Q. Zheng, Z. Guo, C. Wang, Z. Hao, X. Liu, G. Wang, W. Yan, H. Chen and C. Lu, *Adv. Funct. Mater.*, 2021, **31**, 1–15, DOI: **10.1002/adfm.202005732**.
5 X. Li, Y. Cong, M. Ovais, M. B. Cardoso, S. Hameed, R. Chen, M. Chen and L. Wang, *Wiley Interdiscip. Rev.: Nanomed. Nanobiotechnology*, 2023, **15**, 1–25, DOI: **10.1002/wnan.1836**.
6 S. Choudhary, J. V. N. Sarma, S. Pande, S. Ababou-Girard, P. Turban, B. Lepine and S. Gangopadhyay, *AIP Adv.*, 2018, **8**(5), 055114, DOI: **10.1063/1.5028407**.
7 T. Chang, R. P. Babu, W. Zhao, C. M. Johnson, P. Hedström, I. Odnevall and C. Leygraf, *ACS Appl. Mater. Interfaces*, 2021, **13**, 49402–49413, DOI: **10.1021/acsami.1c14253**.
8 D. P. Linklater, V. A. Baulin, X. Le Guével, J. B. Fleury, E. Hanssen, T. H. P. Nguyen, S. Juodkazis, G. Bryant, R. J. Crawford, P. Stoodley and E. P. Ivanova, *Adv. Mater.*, 2020, **32**, 1–15, DOI: **10.1002/adma.201905732**.
9 E. P. Ivanova, D. P. Linklater, M. Werner, V. A. Baulin, X. M. Xu, N. Vrancken, S. Rubanov, E. Hanssen, J. Wandiyanto, V. K. Truong, A. Elbourne, S. Maclaughlin, S. Juodkazis and R. J. Crawford, *Proc. Natl. Acad. Sci. U. S. A.*, 2020, **117**, 12598–12605, DOI: **10.1073/pnas.1916680117**.
10 M. Mu, S. Liu, W. DeFlorio, L. Hao, X. Wang, K. S. Salazar, M. Taylor, A. Castillo, L. Cisneros-Zevallos, J. K. Oh, Y. Min and M. Akbulut, *Langmuir*, 2023, **39**, 5426–5439, DOI: **10.1021/acs.langmuir.3c00043**.
11 G. Sotgiu, S. De Santis, M. Orsini, I. Bavasso, F. Sarasini and E. Petrucci, *ACS Appl. Mater. Interfaces*, 2024, **16**, 24483–24493, DOI: **10.1021/acsami.3c03246**.
12 D. Huo, F. Wang, F. Yang, T. Lin, Q. Zhong, S. P. Deng, J. Zhang, S. Tan and L. Huang, *J. Mater. Sci. Technol.*, 2024, **179**, 208–223, DOI: **10.1016/j.jmst.2023.07.038**.
13 Y. Wu, W. Wu, W. Zhao and X. Lan, *Surf. Coat. Technol.*, 2020, **395**, 125911, DOI: **10.1016/j.surfcoat.2020.125911**.
14 Z. Wu, B. Chan, J. Low, J. J. H. Chu, H. W. D. Hey and A. Tay, *Bioact. Mater.*, 2022, **16**, 249–270, DOI: **10.1016/j.bioactmat.2021.10.008**.
15 B. Wang, Z. Wu, S. Wang, S. Wang, Q. Niu, Y. Wu, F. Jia, A. Bian, L. Xie, H. Qiao, X. Chang, H. Lin, H. Zhang and Y. Huang, *Mater. Sci. Eng. C*, 2021, **128**, 112322, DOI: **10.1016/j.msec.2021.112322**.
16 M. Yamaguchi, H. Abe, T. Ma, D. Tadaki, A. Hirano-Iwata, H. Kanetaka, Y. Watanabe and M. Niwano, *Langmuir*, 2020, **36**, 12668–12677, DOI: **10.1021/acs.langmuir.0c02201**.
17 I. C. Turu, S. Bayraktar, B. Akgul, E. Ilhan-Sungur, E. S. Abamor and N. Cansever, *Surf. Coat. Technol.*, 2023, **470**, 129866, DOI: **10.1016/j.surfcoat.2022.129866**.
18 J. Park, A. B. Tesler, E. Gongadze, A. Iglič, P. Schmuki and A. Mazare, *ACS Appl. Mater. Interfaces*, 2024, **16**, 4430–4438, DOI: **10.1021/acsami.3c19715**.
19 L. Suhadolnik, Ž. Marinko, M. Ponikvar-Svet, G. Tavčar, J. Kovač and M. Čeh, *J. Phys. Chem. C*, 2020, **124**, 4073–4080, DOI: **10.1021/acs.jpcc.9b10066**.
20 S. K. W. Ningsih, M. I. Syauqi, R. Wibowo and J. Gunlazuardi, *J. Appl. Electrochem.*, 2024, **54**, 739–756, DOI: **10.1007/s10800-023-01798-8**.
21 A. Roguska, A. Belcarz, T. Piersiak, M. Pisarek, G. Ginalska and M. Lewandowska, *Eur. J. Inorg. Chem.*, 2012, 5199–5206, DOI: **10.1002/ejic.201200613**.
22 Z. K. He, Y. Lu, C. Zhao, J. Zhao, Z. Gao and Y. Y. Song, *Appl. Surf. Sci.*, 2021, **567**, 150832, DOI: **10.1016/j.apsusc.2021.150832**.
23 Y. Zhuang, P. Li, L. Qin, S. Zhang, B. Chen, Y. Zhu, B. Wang and X. Zhu, *J. Phys. Chem. C*, 2024, **128**, 5741–5748, DOI: **10.1021/acs.jpcc.3c10275**.

24 A. Al-Zubeidi, F. Stein, C. Flatebo, C. Rehbock, S. A. Hosseini Jebeli, C. F. Landes, S. Barcikowski and S. Link, *ACS Nano*, 2021, **15**, 8363–8375, DOI: **10.1021/acsnano.1c01416**.

25 J. Park, D. Kim, H. Kim, W. I. Park, J. Lee and W. Chung, *ACS Omega*, 2022, **7**, 19021–19029, DOI: **10.1021/acsomega.2c02777**.

26 M. Zhang, R. Peltier, M. Zhang, H. Lu, H. Bian, Y. Li, Z. Xu, Y. Shen, H. Sun and Z. Wang, *J. Mater. Chem. B*, 2017, **5**, 5311–5317, DOI: **10.1039/C7TB01468D**.

27 J. Ge, J. Lei and R. N. Zare, *Nat. Nanotechnol.*, 2012, **7**, 428–432, DOI: **10.1038/nnano.2012.93**.

28 A. F. Soares-Filho, R. P. Sousa, R. B. Lima, L. F. G. Noleto, J. F. Cruz-Filho, G. O. M. Gusmão and G. E. Luz, *Opt. Mater.*, 2024, **157**, 116180, DOI: **10.1016/j.optmat.2024.116180**.

29 C. Zhang, X. Ma, J. Xue, S. Liu, C. Feng, J. Han, J. Wu, L. Wang and Y. Wang, *Langmuir*, 2024, **40**, 8981–8991, DOI: **10.1021/acs.langmuir.3c01302**.

30 Y. Bao, W. Fu, H. Xu, Y. Chen, H. Zhang and S. Chen, *CrystEngComm*, 2022, **24**, 1085–1093, DOI: **10.1039/D1CE01345D**.

31 M. Waqas, L. Wang, Y. Hui, F. Fan, Y. Fan, G. Yasmeen, M. Ashraf and W. Chen, *Electrochim. Acta*, 2023, **462**, 142737, DOI: **10.1016/j.electacta.2023.142737**.

32 G. He, W. Hu and C. M. Li, *Colloids Surf. B Biointerfaces*, 2015, **135**, 613–618, DOI: **10.1016/j.colsurfb.2015.08.049**.

33 Y. Bian, X. Chen and Z. J. Ren, *Environ. Sci. Technol.*, 2020, **54**, 9116–9123, DOI: **10.1021/acs.est.0c02402**.

34 D. Guan and Y. Wang, *Nanoscale*, 2012, **4**, 2968–2977, DOI: **10.1039/C2NR11895C**.

35 Y. Yu, Q. Ran, X. Shen, H. Zheng and K. Cai, *Colloids Surf. B Biointerfaces*, 2020, **185**, 110592, DOI: **10.1016/j.colsurfb.2019.110592**.

36 A. S. Gnedenkov, S. L. Sinebryukhov, V. S. Filonina, N. G. Plekhova and S. V. Gnedenkov, *J. Magnes. Alloy*, 2022, **10**, 3589–3611, DOI: **10.1016/j.jma.2022.06.001**.

37 Y. Xu, L. Tan, Q. Li, X. Zheng and W. Liu, *Environ. Technol. Innov.*, 2022, **27**, 102379, DOI: **10.1016/j.eti.2022.102379**.

38 L. Macomber, C. Rensing and J. A. Imlay, *J. Bacteriol.*, 2007, **189**, 1616–1626, DOI: **10.1128/JB.01313-06**.

39 K. N. D. Bandara, K. M. D. C. Jayathilaka, D. P. Dissanayake and J. K. D. S. Jayanetti, *Appl. Surf. Sci.*, 2021, **561**, 150020, DOI: **10.1016/j.apsusc.2021.150020**.

40 Y. Ding, Y. Li, L. Yang, Z. Li, W. Xin, X. Liu, L. Pan and J. Zhao, *Appl. Surf. Sci.*, 2013, **266**, 395–399, DOI: **10.1016/j.apsusc.2012.12.125**.

41 K. Maghsoudi, G. Momen and R. Jafari, *Appl. Mater. Today*, 2023, **34**, 101893, DOI: **10.1016/j.apmt.2023.101893**.

42 R. M. Arán-Ais, R. Rizo, P. Grosse, G. Algara-Siller, K. Dembélé, M. Plodinec, T. Lunkenbein, S. W. Chee and B. R. Cuenya, *Nat. Commun.*, 2020, **11**, 3489, DOI: **10.1038/s41467-020-17220-6**.

43 K. J. Heo, J. H. Yoo, J. Shin, W. Huang, M. K. Tiwari, J. H. Jung, I. P. Parkin, C. J. Carmalt and G. B. Hwang, *J. Mater. Chem. A*, 2024, **12**, 3886–3895, DOI: **10.1039/D3TA08539D**.

44 N. Li, Z. Xu, S. Zheng, H. Dai, L. Wang, Y. Tian, Z. Dong and L. Jiang, *Adv. Mater.*, 2021, **33**(25), 2003559, DOI: **10.1002/adma.202003559**.

45 I. Atalay and F. R. Erişen, *Aust. Endod. J.*, 2023, **49**, 71–78, DOI: **10.1111/aej.12647**.

46 C. Molteni, H. K. Abicht and M. Solioz, *Appl. Environ. Microbiol.*, 2010, **76**, 4099–4101, DOI: **10.1128/AEM.02927-09**.

47 M. D'Accolti, D. Bellotti, E. Dzień, C. Leonetti, S. Leveraro, V. Albanese, E. Marzola, R. Guerrini, E. Caselli, M. Rowińska-Żyrek and M. Remelli, *Sci. Rep.*, 2023, **13**, 1–13, DOI: **10.1038/s41598-022-24748-6**.

48 X. Chen, J. Zhou, Y. Qian and L. Z. Zhao, *Mater. Today Bio*, 2023, **19**, 100586, DOI: **10.1016/j.mtbio.2023.100586**.

49 M. Hans, A. Erbe, S. Mathews, Y. Chen, M. Solioz and F. Mücklich, *Langmuir*, 2013, **29**, 16160–16166, DOI: **10.1021/la4036617**.

50 W. L. Du, S. S. Niu, Y. L. Xu, Z. R. Xu and C. L. Fan, *Carbohydr. Polym.*, 2009, **75**, 385–389, DOI: **10.1016/j.carbpol.2008.07.032**.